

A screening of results on the decay length in concentrated electrolytes†

Henrik Jäger,  ^{‡a} Alexander Schlaich,  ^{‡ab} Jie Yang, ^{bc} Cheng Lian,  Svyatoslav Kondrat  ^{bd} and Christian Holm  ^{*b}

Received 17th February 2023, Accepted 27th April 2023

DOI: 10.1039/d3fd00043e

Screening of electrostatic interactions in room-temperature ionic liquids and concentrated electrolytes has recently attracted much attention as surface force balance experiments have suggested the emergence of unanticipated anomalously large screening lengths at high ion concentrations. Termed underscreening, this effect was ascribed to the bulk properties of concentrated ionic systems. However, underscreening under experimentally relevant conditions is not predicted by classical theories and challenges our understanding of electrostatic correlations. Despite the enormous effort in performing large-scale simulations and new theoretical investigations, the origin of the anomalously long-range screening length remains elusive. This contribution briefly summarises the experimental, analytical and simulation results on ionic screening and the scaling behaviour of screening lengths. We then present an atomistic simulation approach that accounts for the solvent and ion exchange with a reservoir. We find that classical density functional theory (DFT) for concentrated electrolytes under confinement reproduces ion adsorption at charged interfaces surprisingly well. With DFT, we study confined electrolytes using implicit and explicit solvent models and the dependence on the solvent's dielectric properties. Our results demonstrate how the absence vs. presence of solvent particles and their discrete nature affect the short and long-range screening in concentrated ionic systems.

1 Introduction

Electrolytes and ionic liquids (ILs) are virtually everywhere. In biological systems, electrolytes and electrostatic interactions play a crucial role in nearly all processes,

^a*Stuttgart Center for Simulation Science (SC SimTech), University of Stuttgart, 70569 Stuttgart, Germany*

^b*Institute for Computational Physics, University of Stuttgart, Stuttgart, Germany. E-mail: svyatoslav.kondrat@gmail.com; skondrat@ichf.edu.pl; holm@icp.uni-stuttgart.de*

^c*School of Chemistry and Molecular Engineering, East China University of Science and Technology, Shanghai 200237, China*

^d*Institute of Physical Chemistry, Polish Academy of Sciences, 01-224 Warsaw, Poland*

† Electronic supplementary information (ESI) available: Further details on the simulation methods, atomistic simulations, chemical potential measurement and determination of the dielectric constant in the solvent-explicit DFT calculations. See DOI: <https://doi.org/10.1039/d3fd00043e>

‡ These authors contributed equally to this work.



regulating the osmotic pressure and the body's water content,^{1,2} controlling enzymatic cascade reactions,^{3,4} transmitting nerve signals,^{5,6} contracting muscles,⁷⁻⁹ etc. The role of ILs in industrial applications is also hard to overestimate.^{10,11} Ions and electrostatic interactions are essential in applications as diverse as capacitive energy storage¹²⁻¹⁴ and conversion,^{12,15} sensors,¹⁶ and catalysis.^{17,18}

Despite this broad applicability and extreme importance in fundamental life-sustaining processes, our understanding of ionic interactions, particularly ionic screening, is still incomplete. Ionic interactions are exponentially screened; this so-called Debye screening arises from a cloud of counter-ions surrounding each ion. Formally, it can be obtained using the linearised Poisson–Boltzmann equation, also known as the Debye–Hückel equation. The screening length resulting from this theory is known as the Debye screening length. For monovalent ions, it is given by eqn (1),

$$\lambda_D = \sqrt{\frac{\varepsilon_0 \varepsilon_r k_B T}{e^2 \rho}} = (4\pi \lambda_B \rho)^{-1/2}, \quad (1)$$

where $\rho = \rho_+ + \rho_-$ is the total ion concentration ($\rho_+ = \rho_-$ are the cation and anion concentrations), ε_0 is the vacuum and ε_r the relative permittivity, k_B is the Boltzmann constant and T temperature, e the proton charge, and $\lambda_B = e^2/(4\pi \varepsilon_0 \varepsilon_r k_B T)$ is the Bjerrum length.

This elegant and physically intuitive picture of an ionic screening cloud is, however, only valid for dilute electrolytes and breaks down as the ion density increases. The theory of screening in concentrated electrolytes was developed in the mid-1990s.^{19,20} While it does not provide a simple equation (like eqn (1)) for the screening length ξ , it predicts that ξ increases with ion density (ρ) above the so-called Kirkwood crossover,²¹ a crossover from the monotonic to oscillatory decay of the charge–charge correlation function. Note that the Debye length monotonically decreases with ρ .

Recent surface force balance (SFB) experiments²²⁻²⁴ have challenged our understanding of ionic correlations by reporting unusually large screening lengths, about an order of magnitude larger than predicted by classical theory. Ascribed to the bulk properties of ionic systems, such screening was termed^{25,26} ‘underscreening’ to stress that the interactions are ‘under-screened’ compared to what is expected from classical theories.^{19,20} More recent work^{27,28} named it ‘anomalous underscreening’ meaning that the screening predicted by classical theories already ‘under-screens’ the interactions compared to Debye screening. The experiments in ref. 22–24 have renewed research activities in the field of concentrated electrolytes. Although the origin of anomalous underscreening still needs to be revealed, a new wave of theoretical and simulation work has given us new insight, while also demonstrating gaps in our understanding of the behaviour of concentrated electrolytes.

In the first part of this contribution, we provide a brief overview of experimental studies on underscreening (Section 2.1), discuss classical theories of ionic screening (Section 2.2.1), and review more recent theoretical (Section 2.2.2) and simulation (Section 2.3) studies motivated by the underscreening experiments.²²⁻²⁴ As our overview shows, the main focus of the theoretical and simulation studies has been on ILs and dense electrolytes in bulk, while screening in confined systems and by ion–solvent mixtures received less attention. In



Section 3, we use atomistic simulations and classical density functional (DFT) theory and attempt to fill this gap by studying how solvent and confinement affect the structure and screening in concentrated electrolytes.

2 Brief overview of previous results

2.1 Underscreening experiments

The first report on an unusually long screening length dates back to the last decade. In 2013, Gebbie *et al.*²² studied IL-mediated forces between crossed cylinders using SFB and a $[C_4mim]^+[NTf_2]^-$ ionic liquid, followed by studies of several other ILs²³ in 2015. From the long-range behaviour of the measured forces, these authors extracted screening lengths, ξ , that were about one order of magnitude larger than expected from classical theories.^{19,20,29} They explained these surprising results as ions forming neutral “ion pairs” leading to the Debye-like screening determined by a small fraction of “free” ions, an approach criticised by Perkin *et al.*³⁰ and Lee *et al.*³¹

By systematically analysing screening lengths in different concentrated electrolytes and room temperature ILs, Smith *et al.*²⁴ found that “the electrostatic screening length in concentrated electrolytes increases with concentration”. While the increase is, in principle, in agreement with classical theories^{19,20,29} (cf. Fig. 2), the repeatedly measured large values of ξ were surprising and still remain a mystery.³² In follow-up work, Lee *et al.*^{25,26} revealed that all experimental data available at the time collapsed onto a single curve given by eqn (2),

$$\xi/\lambda_D \sim (\sigma_{ion}/\lambda_D)^n \quad (2)$$

with $n = 3$. Fig. 1a shows the data collapse and the cubic scaling. Lee *et al.*²⁶ ascribed this behaviour of the force decay length to the bulk properties of

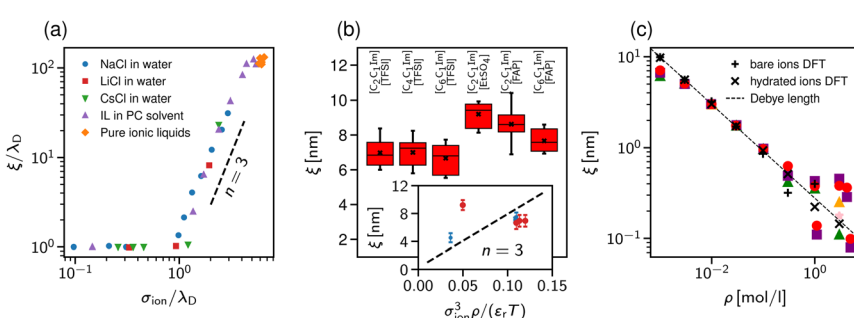


Fig. 1 Ionic screening lengths from experiments. (a) Screening length divided by the Debye length λ_D plotted as a function of the ion diameter σ_{ion} divided by λ_D . The symbols show experimental data for various ionic liquids and aqueous electrolytes collected from ref. 24–26. According to ref. 25 and 26, all values collapse onto a single curve displaying cubic scaling, eqn (2) with $n = 3$, for $\sigma_{ion}/\lambda_D \geq 1$. (b) Screening lengths of six ionic liquids from ref. 36. The inset shows the screening lengths as a function of $\sigma_{ion}^3 \rho / (\epsilon_r T)$, which follows from eqn (2) with $n = 3$, demonstrating deviation from the cubic scaling. (c) Screening lengths vs. ion concentration from ref. 28. The filled symbols show atomic force microscopy (AFM) results for various electrolytes. The black dash line corresponds to the expected Debye length and the crosses and pluses to the DFT results (see Section 2.2.2) with hydrated and bare ion diameter, respectively.



concentrated ionic systems. Thus, with a few exceptions,^{33,34} most theoretical and simulation studies aimed at explaining underscreening, have focused on bulk electrolytes (Sections 2.2 and 2.3).

The authors of ref. 26 explained underscreening as the emergence of charged defects in an overall neutral, nearly crystalline IL. However, as noted by Adar *et al.*,³⁵ this physical picture is only applicable at concentrations above ≈ 5 M, while the experiments show cubic scaling at much lower concentrations. To link underscreening to the bulk properties of electrolytes, Lee *et al.*^{25,26} related the large screening lengths to other experimentally measurable quantities, *viz.* excess chemical potential, μ_{ex} , and differential capacitance, C_d . However, Zeman *et al.*³³ criticised this relation by showing that 'screening lengths' extracted from the experimental data on μ_{ex} and C_d using the models proposed in ref. 25 and 26 disagree with the screening lengths measured experimentally in ref. 22–24.

The experiments of ref. 22–24 have motivated several studies on other ILs and concentrated electrolytes using various experimental techniques. While most of the published studies support underscreening,^{37,38} there are also studies reporting either large ξ but no cubic scaling³⁶ or no anomalously large screening lengths at all;^{28,39} examples are shown in Fig. 1b and c, respectively.

2.2 Theory

2.2.1 Classical theories. Screening in concentrated ionic systems was actively investigated in the mid-1990s. Attard¹⁹ studied charged hard spheres (restricted primitive model, RPM) using the Ornstein–Zernike equation and the hypernetted chain closure. By analysing the asymptotic behaviour of pair correlation functions, he identified three regimes. At low ion concentrations, the (charge–charge) correlation function decays monotonically exponentially, with the decay length close to the Debye length λ_D , but becoming progressively smaller than λ_D as the concentration increases. Above the concentration known as the Kirkwood crossover,²¹ there are two damped oscillatory regimes, electrostatics dominated at

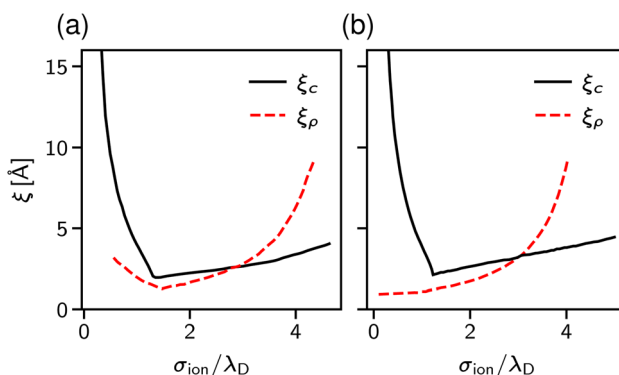


Fig. 2 Ionic screening lengths from classical theories. In both plots, the screening lengths are plotted as functions of the ion diameter divided by the Debye length λ_D . The largest screening length determines the asymptotic behaviour. The solid and dotted lines show the screening lengths due to electrostatic and hard-core domination, respectively. (a) Ornstein–Zernike equation and the hypernetted chain closure by Attard¹⁹ and (b) generalised mean spherical approximation by de Carvalho and Evans.²⁰



intermediate concentrations and hard-core dominated at high concentrations, as determined by the largest decay length. The decay length ξ as a function of $\sigma_{\text{ion}}/\lambda_D$ is shown in Fig. 2a. We stress that above the Kirkwood cross-over, ξ increases with concentration. de Carvalho and Evans²⁰ used the generalised mean spherical approximation (MSA) for the RPM and obtained similar results (Fig. 2b).

2.2.2 Recent theories. The underscreening experiments (Section 2.1) rekindled interest in ionic screening, and several approaches have been developed in an attempt to explain the unusually large screening lengths.^{34,35,40–43} Rotenberg *et al.*⁴⁰ considered primitive (RPM) and ‘semi-primitive’ (charged hard spheres and hard-sphere solvent) models. They applied MSA to compute the charge–charge correlation functions and found that, in line with previous work,^{19,20} the screening length increased with concentration for concentrations above the Kirkwood cross-over. Interestingly, the rate of increase, *i.e.*, the scaling exponent in eqn (2), depends on the model. The primitive model shows $n = 3/2$, while the semi-primitive model yields $n = 1$ (Fig. 3a).

Adar *et al.*³⁵ calculated the charge–charge correlation function on the Gaussian level, but modified the Coulomb kernel to account for the excluded volume interactions between neighbouring ions. These authors considered two ion models: a homogeneously charged sphere and a homogeneously charged spherical shell. They found that, above the Kirkwood point, the decay length of the charge–charge correlation function increases with the concentration with the scaling exponent $n = 2$ for both models (Fig. 3b).

Cats *et al.*³⁴ used DFT^{44–46} with various MSA-like approximations for the electrostatic interactions and fundamental measure theory (FMT)^{47–50} for hard core interactions to study charge and total density correlation functions of the RPM. Above the Kirkwood point, they found an increasing decay length dominated by

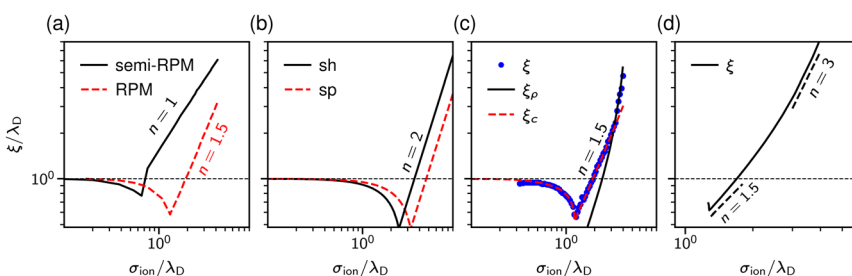


Fig. 3 Theoretical predictions for ionic screening lengths. In all plots, the screening lengths are divided by the Debye length λ_D and plotted as a function of the ion diameter divided by λ_D . (a) Mean spherical approximation for an ionic liquid (black solid line), described by a restricted primitive (RPM) model, and an ionic liquid–solvent mixture (red dashed line), modelled as charged and neutral hard spheres (semi-RPM). Note the different scaling exponents $n = 1$ and $n = 3/2$. Data from ref. 40. (b) Extended mean field theory modified to account for ion sizes³⁵ predicts a quadratic scaling (‘sh’ and ‘sp’ denote spherical shell and homogeneous sphere models for ions). (c) DFT results for the decay length of the solvation force compared to the decay lengths of the total and charge density profiles at a wall (ξ_p and ξ_c). Data from ref. 34. (d) Results of the Ciach–Patsahan theory showing that exponent n changes continuously from $n = 1.5$ close to the Kirkwood point to $n = 3$ for $2.5 \leq \sigma_{\text{ion}}/\lambda_D \leq 4$. Note that the x -axis has a different range than the other panels. Data from ref. 41.



electrostatics and the scaling exponent $n = 1.5$, which seems to be characteristic of the MSA for the primitive model.⁴⁰ In line with Attard¹⁹ and de Carvalho and Evans,²⁰ they saw a cross-over to the hard-core dominated screening as the concentration increased (Fig. 3c).

In contrast to previous work that reported scaling exponents $n < 3$, Ciach and Patsahan^{42,43} arrived at an exponent $n = 3$ using a self-consistent Gaussian approximation based on the Brazovskii approach.^{51,52} Unlike previous theoretical approaches, these authors took into account the local variance of the charge density. However, similar to the phenomenology of ref. 25 and 26, their theory appears to be valid only at unusually high concentrations (e.g., above $\approx 23 \text{ mol l}^{-1}$ for aqueous sodium chloride and $\approx 5 \text{ mol l}^{-1}$ for room temperature ILs taking bare ion diameters, see ref. 33). We recall that experimentally the cubic scaling was reported at much lower concentrations ($\approx 1 \text{ mol l}^{-1}$).

In more recent work, Ciach and Patsahan⁴¹ found that the exponent n is not constant but varies with $\sigma_{\text{ion}}/\lambda_D$ from $n = 1.5$ close to the Kirkwood point to $n = 3$ for $2.5 \leq \sigma_{\text{ion}}/\lambda_D \leq 4$, increasing further for $\sigma_{\text{ion}}/\lambda_D > 4$ (Fig. 3d). These authors also found two other exponents $n = 1$ and $n = 5$, but for the density-density decay length.⁴¹

The cubic scaling in ref. 41–43 emerged in the damped oscillatory decay of the charge–charge correlation function. In experiments, however, the force exhibiting large screening lengths with cubic scaling decayed monotonically with distance between the surfaces. Kjellander^{53,54} showed the possibility of long-range monotonic decay at high densities using dressed ion theory.^{55,56} However, to our knowledge, this approach is yet to be applied to experimental or simulation data of ionic systems with anomalously large screening lengths and cubic scaling.

2.3 Simulations

Studying underscreening with molecular simulations is challenging because huge boxes and long simulation runs must be considered to capture the possible appearance of the experimentally measured large screening lengths. Coles *et al.*⁵⁷ studied aqueous LiCl and NaI, and lithium bis(trifluoromethane)sulfonimide [Li][TFSI] in water and an organic solvent mixture of dimethoxyethane and dioxolane. By analysing the charge–charge correlation functions, they found that the decay length increases with concentration, and reported a scaling exponent $n \approx 1.3$ (Fig. 4a). We note, however, that these authors studied simulation systems with box lengths from about 9 nm to 11 nm. The monotonic underscreening decay was reported for separations between 4 and 7 nm for ILs (screening lengths from 2 nm to 10 nm) and up to 3 nm for aqueous NaCl (screening lengths from 1 nm to 3 nm).^{22–24} The simulated systems were, therefore, at the edge or even too small for the underscreening regime.

Zeman *et al.*^{33,58} studied aqueous NaCl with all-atom simulations and 1-butyl-3-methylimidazolium hexafluorophosphate ($[\text{C}_4\text{C}_1\text{Im}][\text{PF}_6]$) with both all-atom and coarse-grained simulations. They considered simulation box sizes from about 10 nm to 50 nm, depending on the system, to allow the evaluation of potentials of mean-force (PMF) at experimentally relevant distances. They did not find any sign of underscreening down to the accuracy of $10^{-5} k_B T$ in the PMF. Instead, they revealed a crossover between the scaling with exponent $n = 1$ and $n = 2$ (Fig. 4b).



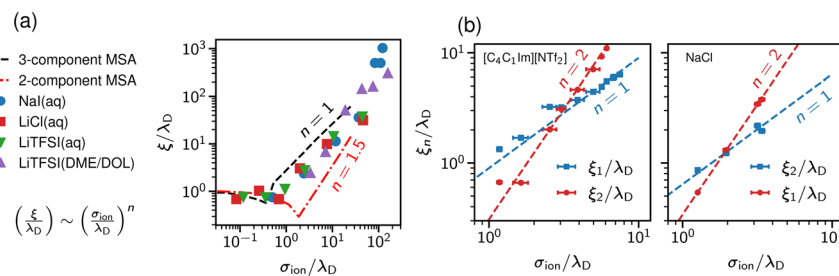


Fig. 4 Screening lengths from molecular dynamics simulations. (a) Simulation results for a few ionic liquids and aqueous electrolytes obtained by Coles *et al.*⁵⁷ MSA results are displayed for comparison. The MSA results are shown for the restricted primitive model (RPM) and the RPM with non-polar solvent of the same size as the ions. The simulation results show scaling given by eqn (2) with $n \approx 1.3$. (b) Large-scale simulation results for 1-butyl-3-methylimidazolium bis(trifluoromethanesulfonyl)-imide ($[C_4C_1Im][NTf_2]$, left plot) and aqueous NaCl (right plot). Data from ref. 58.

Zeman *et al.*³³ also studied confined $[C_4C_1Im][PF_6]$ and found that the screening lengths obtained from the density and electric field profiles are in good quantitative agreement with the bulk simulations.

The semi-primitive electrolyte model was considered with MD simulations by Coupette *et al.* Unlike classical theories (Fig. 2) and DFT calculations (Fig. 3c), which predict a crossover from the electrostatics to hard-core dominated screening regime (above the Kirkwood cross-over), they found a crossover in the reverse order, *i.e.*, from the hard-core to an electrostatics dominated regime upon increasing ion concentration. In their most recent work, Härtel *et al.*²⁷ studied the primitive electrolyte model and reported anomalously large screening lengths. However, these authors considered a strong coupling regime (large Bjerrum lengths), leading to the formation of ionic clusters even at low densities and Debye-like screening determined by ‘free’ ions. It remains to be seen if this picture stays valid in an experimentally relevant weak coupling regime.

3 How surfaces, confinement and solvent influence the ionic structure and screening

As we see from this brief overview, the main focus of theory and simulations has been on bulk ILs and electrolytes, motivated by the claim that underscreening is a bulk property of concentrated ionic systems. However, how and on which length scale does the presence of surfaces and confinement modify ionic screening? In simulations of confined fluids, one usually fixes the number of species (*i.e.*, the number of solvent and salt molecules in the case of electrolytes) to the corresponding densities in bulk, which might differ considerably in confinement. These issues have been addressed for all-atom simulations only in the case of salt-free simulations (*i.e.*, only counter-ions screening the surface charge and no salt) using for example grand-canonical Monte Carlo (GCMC) simulations⁶⁰ or advanced free energy perturbation (FEP)⁶¹ to extrapolate to the bulk chemical potential,⁶² depending on the desired accuracy. For example, water GCMC simulations are known to converge slowly at an accuracy of ± 1 solvent



molecules,⁶³ an issue which is even more complicated for complex ILs. In Section 3.1.1, we extend our previously established thermodynamic extrapolation approach to control the water chemical potential^{63–65} to a simultaneous extrapolation of the solvent and salt chemical potentials based on FEP and apply it to a confined electrolyte.

Another question that previous studies have neglected is the effect of solvent. While solvent was present in some atomistic simulations,^{33,57,58} a systematic understanding of the role of solvent in electrostatic screening is still lacking. In theoretical approaches and coarse-grained simulations,^{40,59} solvent molecules were modelled as non-polar neutral hard spheres, while a constant relative dielectric permittivity, independent of the local ion and solvent density, described the dielectric properties of the solvent. But how does the structure of a polar solvent, which directly screens the ion–ion interactions, affect ionic screening? In this section, we first employ atomistic molecular simulations at a prescribed chemical potential to study how surface and confinement effects can modify the composition of an aqueous electrolyte (NaCl) confined between accurately modelled mica sheets (Fig. 5a). Density functional theory (DFT) calculations using an explicit solvent model (Fig. 5b) reveal systematic surface depletion of the salt and solvent density profiles that both agree remarkably well with MD simulations. We then use an implicit solvent model (Fig. 5c) to investigate the effect of spatially resolving solvent molecules on the ionic screening and the structure of confined ILs.

3.1 Methods

3.1.1 Atomistic MD simulations. We employ atomistic molecular dynamics simulations to obtain detailed microscopic insight into the solvent and

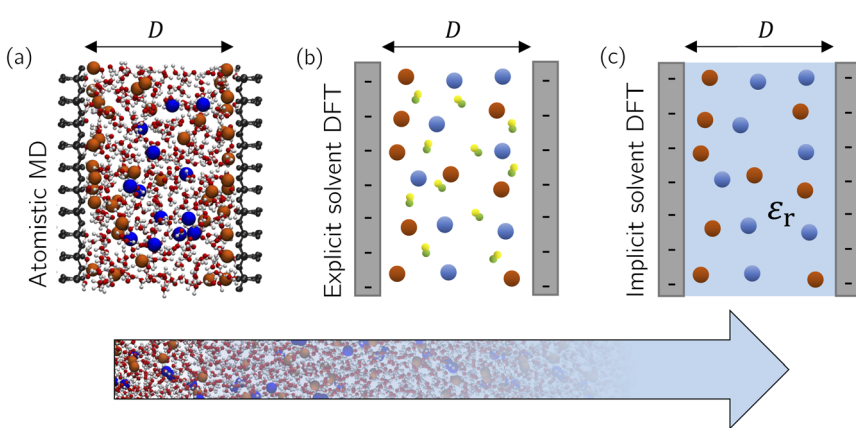


Fig. 5 Modelling approaches ranging from atomistic simulations to implicit solvent DFT calculations. (a) Snapshot of the atomistic simulation system. Water (small red and white spheres show oxygen and hydrogen, respectively) together with the electrolyte ions (large orange and blue spheres show sodium and chloride, respectively) are confined between mica sheets separated by a distance D between the outermost mica atoms. Schematics of two charged plates confining an electrolyte with explicit (b) and implicit (c) solvent models. Cations and anions have the same diameter σ_{ion} and solvent molecules consist of two oppositely charged beads of the same diameter σ_s . The plate separation is D in both models.



electrolyte structures. In particular, we study an aqueous salt solution (NaCl) confined between infinite, parallel mica surfaces. A dioctahedral muscovite T-O-T double layer ($\text{KAl}_2[(\text{OH})_2 \text{AlSi}_3\text{O}_{10}]$) is taken from the InterfaceFF force field package,⁶⁶ which is expected to reproduce the experimental data exceptionally well due to its parametrisation based on structural and interfacial energy aspects. The studied mica double layer (Fig. 6a) has lateral dimensions of about $2.9 \text{ nm} \times 3 \text{ nm}$. One layer was then displaced to form a slit pore, where we consider a fixed surface separation based on the outermost mica atoms of $D = 2 \text{ nm}$. Water was modelled using the TIP4P/ ϵ parametrisation⁶⁷ and ions based on a thermodynamically consistent, transferable force field.⁶⁸ See Section S1 in the ESI† for simulation details.

As alluded, the natural choice of the ensemble for the simulation of a confined system is the grand-canonical ensemble, since ions and water molecules can be exchanged with a reservoir in the relevant experimental setups, thus balancing the chemical potentials of the system under investigation with an external reservoir. In practice, grand-canonical approaches for aqueous or IL systems suffer from major convergence problems.⁶³ We build upon the thermodynamic extrapolation method⁶⁴ to determine the correct composition of the confined system, *viz.* the N_s and N_{ion} of solvent and salt species. The key idea is to determine the chemical potential of each species for different system compositions (N_s, N_{ion}), see Section S1 in the ESI.† Thus, the multidimensional optimisation problem of the system composition corresponding to the chemical

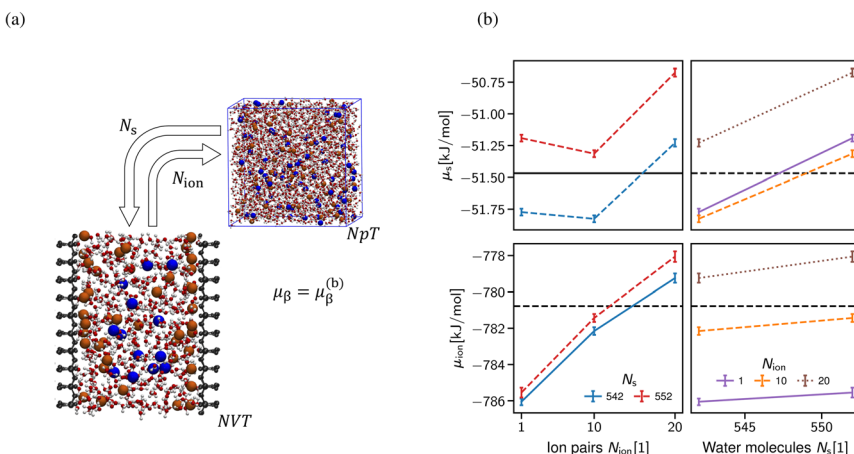


Fig. 6 Extrapolation of the correct system composition. (a) The chemical potential of each species is calculated in the centre of the slit for a range of different system compositions (N_s, N_{ion}). Since the numerical value of the chemical potential is highly dependent on the force field used, we use the reference potentials from molecular dynamics simulations of a bulk electrolyte at given salt concentrations as the baseline. (b) The multidimensional optimisation problem of system composition (N_s, N_{ion}) and chemical potential (μ_s, μ_{ion}) is broken down into independent minimisations in N and μ for each species, as illustrated here for 2 mol l^{-1} . The ion species is largely unaffected by the number of solvent molecules, yet the chemical potential of the solvent species is highly affected by the number of ion pairs. To obtain a usable set of particle numbers, we choose them such that the chemical potential of both species is closest to the reference values corresponding to the desired concentration in the bulk.



potentials (μ_s , μ_{ion}) is transformed into independent relations of $N_\alpha(\mu_\alpha)$ at fixed concentration of all other species (see Fig. 6b). In practice, the inverse problem is solved, *i.e.*, $\mu_\alpha(N_\alpha)|_{\{N_\beta\}}$, determined at a fixed composition of all other species (β) to extrapolate the particle numbers that correspond to the desired chemical potential in bulk at a given salt concentration. The non-monotonic behaviour of the chemical potential of water observed in Fig. 6b in general makes the extrapolation difficult to apply. However, the chemical potential of the ion pairs is largely independent of the number of solvent molecules, *i.e.* the water chemical potential can be tuned once a suitable number of ion pairs has been chosen.

A clear disadvantage of this approach is its computational cost, since the uncertainty in the chemical potentials must be very small (in the order of $0.01 k_B T$) to reliably predict the composition as shown in Fig. 6b. This requires simulation times of >100 ns per FEP state (Section S1 in the ESI†), thus amounting to at least $5 \mu\text{s}$ for each data point shown in Fig. 6b. For this reason, we limit the application of this approach to only determine the correct composition of a single system size $D = 2 \text{ nm}$, which then yields the desired chemical composition and thus allows for meaningful comparison with the classical DFT calculations shown in Section 3.2.1. Note that (i) the extraction of density oscillation decay lengths requires significantly larger simulation boxes⁵⁸ and (ii) obtaining the pressure decay length requires a significant number of different slit sizes D .

3.1.2 DFT. We consider ions as charged hard spheres of equal diameter $\sigma_{\text{ion}} = 0.5 \text{ nm}$ and valence $Z_+ = Z_- = 1$ and treat the solvent as a dielectric medium with relative dielectric constant ϵ_r , *i.e.*, we describe the electrolyte with an RPM. However, we also consider an explicit solvent model with solvent molecules modelled as dimers consisting of two hard spheres of diameter $\sigma_{s+} = \sigma_{s-} = 0.2 \text{ nm}$ and opposite charge $q_s = 0.1926$ separated by a distance of 0.2 nm , resulting in a dipole moment of 1.85 D . This model was previously introduced by Henderson *et al.*⁶⁹

The interaction potential between a pair of charged beads (either solvent or ions), i and j , separated by a distance r , is given by eqn (3),

$$\beta u_{ij}(r) = \begin{cases} \infty, & r < (\sigma_i + \sigma_j)/2 \\ Z_i Z_j \lambda_B / r, & r > (\sigma_i + \sigma_j)/2 \end{cases} \quad (3)$$

where $\beta = 1/k_B T$, with k_B being the Boltzmann constant and T the absolute temperature (we used $T = 293 \text{ K}$ in all DFT calculations), $\lambda_B = \beta e^2 / 4\pi\epsilon_0\epsilon_r$ is the Bjerrum length, with ϵ_0 being the vacuum and ϵ_r the relative dielectric constant. In the explicit solvent model, following Henderson *et al.*,⁶⁹ we set the background dielectric constant $\epsilon_b = 4.1$, which enhances numerical convergence related to strong electrostatic interactions and correspondingly steep density profiles. Note that ϵ_b can be interpreted as scaling all charges by a factor $\approx 1/2$ to reduce the strength of the Coulomb energy. Physically, it describes the electronic and other degrees of freedom of solvent molecules not taken into account explicitly by the model. We used a capacitor setup (Section S2.1 in the ESI†) to estimate the resulting effective dielectric permittivity, $\epsilon_r \approx 2.4 \times \epsilon_b = 9.8$, in a reasonable agreement with MD simulations of an explicit particle-based dumbbell model, yielding $\epsilon_r \approx 4.4 \times \epsilon_b = 18$ (Section S2.2 in the ESI†).



We consider the electrolyte confined between two positively charged walls with surface charge density $Q = 0.5e \text{ nm}^{-2}$. This slit pore with surface-to-surface separation D interacts with species i through the hard-wall potential, as in eqn (4),

$$\beta U_i(z) = \begin{cases} 0 & \sigma_i/2 \leq z \leq D - \sigma_i/2 \\ \infty & \text{otherwise} \end{cases}. \quad (4)$$

Note that the electric field inside the slit is zero, making the wall interaction in eqn (4) independent of the surface charge, which only enters *via* the charge neutrality condition.

Within DFT, the equilibrium density profiles are determined by minimising the grand potential, eqn (5),

$$\begin{aligned} \beta \mathcal{Q} = & \beta F[\rho_s(\mathbf{R}), \{\rho_\alpha(\mathbf{r})\}] + \int [\beta U_s(\mathbf{R}) - \beta \mu_s] \rho_s(\mathbf{R}) d\mathbf{R} \\ & + \sum_{\alpha=\pm} \int [\beta U_\alpha(\mathbf{r}) - \beta \mu_\alpha] \rho_\alpha(\mathbf{r}) d\mathbf{r} \end{aligned} \quad (5)$$

with respect to the ion ($\rho_\alpha, \alpha = \pm$) and solvent (ρ_s) densities. Here μ_s is the solvent chemical potential chosen such that the bulk solvent density is fixed to $\rho_s^{(b)} = 55.6 \text{ mol l}^{-1}$, and μ_α is chosen to yield a given bulk ion concentration. The second term in eqn (5) is present only in the case of explicit solvent; in this second term, $\mathbf{R} \equiv (\mathbf{r}_{s+}, \mathbf{r}_{s-})$ denotes the two coordinates specifying the position of the two beads of the solvent dimer and $U_s(\mathbf{R}) = U_{s+}(\mathbf{r}_{s+}) + U_{s-}(\mathbf{r}_{s-})$.

The total intrinsic Helmholtz free energy F consists of the ideal part and the excess contribution F_{ex} , *i.e.* eqn (6),

$$\begin{aligned} \beta F = & \int [\ln \rho_s(\mathbf{R}) - 1] \rho_s(\mathbf{R}) d\mathbf{R} + \beta \int V_b(\mathbf{R}) \rho_s(\mathbf{R}) d\mathbf{R} \\ & + \sum_{\alpha=\pm} \int [\ln \rho_\alpha(\mathbf{r}) - 1] \rho_\alpha(\mathbf{r}) d\mathbf{r} + \beta F_{\text{ex}}. \end{aligned} \quad (6)$$

The first and second terms are only present in the case of explicit solvent, and V_b is the bonding potential of a (rigid) solvent molecule given by eqn (7)⁷⁰

$$\exp[-\beta V_b(\mathbf{R})] = \frac{\delta(|\mathbf{r}_{s+} - \mathbf{r}_{s-}| - \sigma_{s\pm})}{4\pi\sigma_{s\pm}^2}. \quad (7)$$

The excess Helmholtz free energy F_{ex} consists of different molecular interactions and correlations given by eqn (8)

$$F_{\text{ex}} = F_{\text{ex}}^{\text{hs}} + F_{\text{ex}}^{\text{C}} + F_{\text{ex}}^{\text{el}} + F_{\text{ex}}^{\text{ch}}, \quad (8)$$

where the terms on the right hand side denote the free energy contributions coming from hard sphere repulsion, direct coulombic interaction, electrostatic correlations and chain connectivity, respectively. We used the modified fundamental measure theory (FMT) to model hard-core repulsion^{48,71} and treated electrostatic correlations through the second-order density functional expansion with the first and second order direct correlation function obtained within the



mean spherical approximation.⁷² To account for the chain connectivity, we used the Wertheim's first order thermodynamic perturbation theory.^{73,74}

The Coulomb energy was directly obtained by integrating Poisson's equation, $\nabla^2\psi(\mathbf{r}) = \rho_c(\mathbf{r})/\varepsilon_0\varepsilon_r$, where $\rho_c(\mathbf{r})$ is the local charge density and $\psi(\mathbf{r})$ the local electrostatic potential. For the one-dimensional slab system and using $\psi(z = 0) = \psi(z = D) = \psi_0$, we get eqn (9)

$$\psi(z) = \psi_0 + \frac{e}{\varepsilon_0\varepsilon_r} \left[\frac{z}{D} \int_0^D dz' (D - z') \rho_c(z') - \int_0^z dz' (z - z') \rho_c(z') \right] \quad (9)$$

and the corresponding excess chemical potential is $\beta\mu_{\text{ex},i}^C(z) = eZ_i\psi(z)$.

We solved the Euler–Lagrange equations following from the minimisation of eqn (5) using the conventional Picard iteration method.⁷⁵ We used the bulk concentrations as an initial guess for the density profiles to determine F_{ex} and $\psi(z)$ and performed iterations until a relative accuracy of 10^{-8} in densities at all positions was achieved. Convergence was obtained for discretisation $\Delta z = (1–5) \times 10^{-2} \sigma_s$ depending on the salt concentration and plate separation. We ensured a constant surface charge density Q through appropriate choice of ψ_0 . The interaction pressure was then obtained by numerically differentiating eqn (5), *i.e.*, $P = -\delta(\Omega/A)\delta D$, and the extrapolation of $D \rightarrow \infty$ gave us the corresponding bulk pressures. We note that the bulk values differ for the implicit and explicit solvent models and amount to $\beta\sigma_{\text{ion}}^3 P_b \approx 2.4$ and ≈ 23 , respectively.

3.2 Results

3.2.1 Ion distribution and excess adsorption. Fig. 7 shows the normalised solvent and ion density profiles $\bar{\rho}_\alpha(z) = \rho_\alpha(z)/\rho_\alpha^{(b)}$, obtained using our atomistic MD simulations in a mica slit pore of width $D = 2$ nm. Note that the z -axis is shifted with respect to the Gibbs dividing surface⁷⁶ (GDS) of species j , $z_G^{(j)}$, which

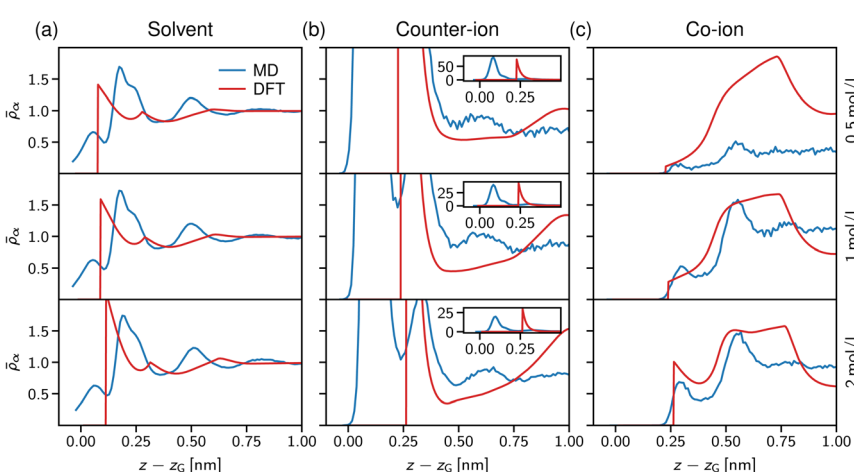


Fig. 7 Normalised solvent and ion densities. (a) Solvent and (b, c) ion density profiles from atomistic MD simulations (blue lines) and solvent-explicit DFT calculations (orange lines). Data is shown for different salt concentrations, 0.5 mol l^{-1} (top), 1.0 mol l^{-1} (centre), and 2.0 mol l^{-1} (bottom), in a slit of width $D = 2$ nm. All data are shifted with respect to the solvent Gibbs dividing surface.



follows from the surface excess of species i with respect to j , as described in eqn (10)

$$\Gamma_{ij} = \int_{-\infty}^{z_G^{(j)}} (\rho_i(z) - \rho_i(z_a)) dz + \int_{z_G^{(j)}}^{\infty} (\rho_i(z) - \rho_i(z_b)) dz, \quad (10)$$

where $\rho_i(z_a) = 0$ and $\rho_i(z_b) = \rho_i^{(b)}$ are the corresponding fluid densities from both sides of the interface, *i.e.* no particles inside the solid and bulk density in the fluid mixture. In the context of ion adsorption, it is convenient to choose the solvent as the reference, $\Gamma_{ss} = 0$, which upon partial integration and dropping the index for the solvent species yields the GDS from eqn (11)

$$z_G = z_a + \int_{z_a}^{z_b} \frac{\rho_s(z_b) - \rho_s(z)}{\rho_s(z_b) - \rho_s(z_a)} dz, \quad (11)$$

with z_a and z_b being reference positions inside the solid and the fluid phase.

In Fig. 7a, the solvent density profiles are shown for concentrations ranging from 0.5 to 2 mol l^{-1} , revealing the well-known layering at solid substrates.⁷⁷ Noteworthy, the atomistic MD data (blue lines) are hardly affected by increasing the salt concentration, with only the third layer getting more pronounced at 2 mol l^{-1} in line with the counter-ion layering in the bottom row of Fig. 7c. On the contrary, the simple dumbbell model employed for the DFT calculations shows increasing layering at the interface for the higher salt concentrations, but also in this case an increase of the third solvent layer density similar to the atomistic data is observed. Note that the atomistically resolved mica sheets have a rough surface according to their chemical structure, thus water can penetrate into the Gibbs surface, $z - z_G < 0$. In contrast, the solvent dumbbells consist of hard spheres of radius 1 Å, in line with the position of the first density peak appearing in Fig. 7a. Regarding the simplicity of this model, the general trends of the solvent structure at the interface are reproduced remarkably well.

We now turn to the structural arrangement of the salt ions, shown in the middle and right columns of Fig. 7. In the atomistic simulation system, sodium counter-ions are employed, which adsorb strongly at the mica surface due to their tendency to release their hydration shell.⁷⁸ However, in the DFT calculations both co- and counter-ions are treated as hard spheres with the same diameter $\sigma_{\pm} = 0.5$ nm. While this leads to a remarkably good agreement for the co-ion profiles (chloride in the atomistic simulations), especially at high concentration (the bottom row in Fig. 7c), the adsorption peak of the counter-ion is not well captured in the DFT calculations. Also note that in the atomistic simulations, mica has a surface charge density that is more than three times larger than in the DFT calculations ($Q = -1.8e \text{ nm}^{-2}$ for mica *vs.* $0.5e \text{ nm}^{-2}$), which explains that the area under the first counter-ion peak differs significantly between both approaches (see insets in Fig. 7b).

Our atomistic simulations indicate that the strong adsorption of sodium strongly screens the mica surface charge, reflected by nearly constant ion density profiles behind the second co-ion density peaks in Fig. 7c. As noted by Graham,⁷⁹ the first strong adsorption layer of the partially hydrated sodium is not captured within the Stern layer of classical double layer theory; correspondingly, the two maxima in the counter-ion density profiles define the inner and outer Helmholtz planes,⁸⁰ which are present also in the solvent-explicit DFT calculations, although



differing significantly in their distance due to the different ion diameter. The co-ion profiles at high concentration (the bottom row in Fig. 7c) agree well for the first two layers and the distance between the two maxima of about 2 nm corresponds to a solvent molecular size. Thus, we conclude that electrostatic and ion-specific effects dominate the magnitude of adsorption, whereas steric effects including the solvent molecules determine the structure close to the interface at charged surfaces.

The specific effects due to adsorption can be further quantified in the context of the Gibbs surface excess, *cf.* eqn (10). In the presence of a charged interface, the counter-ions need to be accounted for explicitly to obtain a thermodynamic consistent interface definition. Taking the solvent as reference for the Gibbs surface allows us to define an effective slit width in a simulation box of length L_z normal to the interface, from eqn (12)

$$D_G = \int_{-L_z/2}^{L_z/2} \frac{\rho_S(z)}{\rho_S^{(b)}} dz. \quad (12)$$

Using the ion pair density $\rho = \rho_+ + \rho_-$, the salt surface excess then directly follows from eqn (10) to give eqn (13)

$$\Gamma = \int_{-D_G/2}^{D_G/2} [\rho(z) - \rho^{(b)}] dz - 2Q/e, \quad (13)$$

which we defined such that it equals zero when the ion density is constant and equals to the bulk ion density. Fig. 8a shows the resulting ion pair surface excess as a function of the effective slit width D obtained from solvent-explicit DFT calculations. A damped oscillatory behaviour is observed for Γ related to ion layering and “quantised” expulsion of ionic layers with decreasing D .⁸¹ Whereas such layering effects are nearly absent for low concentrations, the oscillation amplitude as well as the range of surface separations D at which such oscillations can be observed increases with concentration (see also Fig. 8b). The negative surface excess observed in the slit can be attributed to the Donnan effect:⁸²

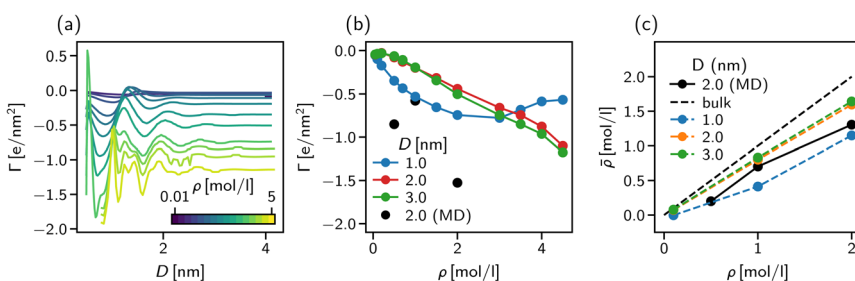


Fig. 8 Surface excess and effective concentration in solvent-explicit simulations. (a) Surface excess of ionic species in the explicit DFT model as a function of slit width. The excess is calculated with respect to the Gibbs dividing surface of the solvent species. (b) Surface excess of ionic species in the explicit DFT model as a function of bulk concentration. The three black points represent the results of the molecular dynamics simulations. (c) Effective concentration of the ionic species inside the slit as a function of bulk concentration.



counter-ions and the presence of charged interfaces dominate the electrostatic interactions, making it unfavourable for salt ions to enter the confined area.

The strong negative surface excess is qualitatively confirmed by our atomistic MD simulations, shown in Fig. 8b as block circles for the three concentrations considered. Whereas the DFT calculations only show a non-monotonic behaviour of Γ vs. the bulk concentration, the surface excess is expected to reveal a more complex behaviour for the atomistic system since ion-specific effects and molecular degrees of freedom are not taken into account in our DFT calculations.

The importance of addressing the solvent composition in confinement is highlighted in Fig. 8c, where we show the solvent composition in terms of the effective concentration $\bar{\rho} = N_{\text{ion}}/N_s$ in the pore vs. the corresponding value in bulk for different slit width D . The bisector corresponds to the trivial assumption of equal amounts of salt inside the pore as in the bulk. The fact that for increasing bulk concentration, $\bar{\rho}$ deviates more strongly from the bisector, can be explained by the increasing surface excess as shown in Fig. 8a and b. The deviation between the trivial assumption and the actual salt ion number is up to a factor of two for $D = 1$ nm. Thus, to compare atomistic simulations of confined complex liquids to experimental data or theoretical models, the chemical potential of all species needs to be controlled carefully. While the approach presented here is capable of determining the right composition at high accuracy, its severe computational cost renders it unfeasible for practical application such as the study of underscreening in the pressure decay length. We found, however, that our solvent-explicit DFT calculations reproduce remarkably well the qualitative behaviour of atomistic simulations employing the extrapolation of chemical potentials for mixture compositions. Thus, we use in the next section solvent-explicit and -implicit DFT calculations to study the influence of an explicit solvent on ionic screening.

3.2.2 Screening lengths. We now discuss how the decay length ξ of an electrolyte-mediated force between confining walls depends on the properties of a solvent. To this end, we performed DFT calculations with an explicit and implicit solvent model characterised by the same relative dielectric permittivity $\varepsilon_r = 9.8$. For the implicit solvent we also consider various ε_r . To extract ξ , we fitted the DFT data for the pressure (*i.e.* force per surface area) at large plate–plate separation to eqn (14)

$$P(D) \approx P_b + A e^{-D/\xi} \cos(2\pi D/\Lambda + \phi), \quad (14)$$

where A is the amplitude, and Λ and ϕ are the period of oscillations and the phase shift, respectively. We treated ξ , Λ , A , and ϕ as the fitting parameters.

The results are shown in Fig. 9. Panel (a) of this figure demonstrates that, perhaps surprisingly, the implicit and explicit solvent models lead to the same values of the decay lengths ξ . The agreement is due to the fact that, in this regime, the screening is determined by electrostatic interactions, which are the same in both models. In line with earlier work, the screening length increases and shows the scaling behaviour given by eqn (2) with exponent $n = 1.5$.^{34,40}

Since both models lead to the same screening lengths, we consider only the implicit solvent model in the following. Fig. 9b shows the screening lengths for different values of ε_r . This figure demonstrates that ξ is independent of ε_r for intermediate concentrations, but there are systematic deviations as the concentration increases.



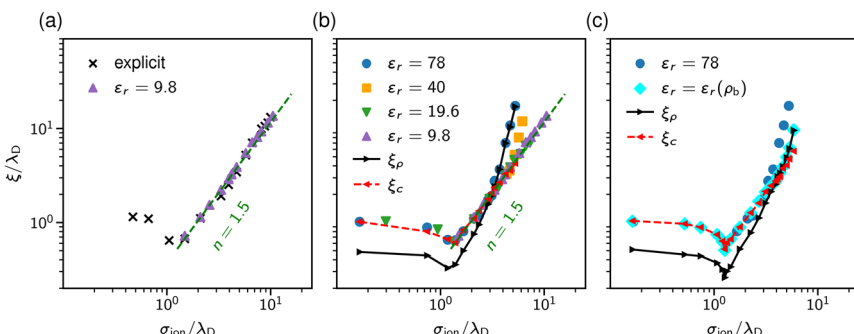


Fig. 9 Screening lengths from DFT. Screening lengths are divided by the Debye length λ_D and plotted as a function of the ion diameter divided by λ_D . (a) Screening lengths for an explicit and implicit solvent model with the same relative dielectric permittivity $\epsilon_r = 9.8$. (b) Screening lengths for several values of ϵ_r . The black and red symbols and lines show the decay lengths of the total and charge density profiles at a single wall for $\epsilon_r = 78$. (c) Screening lengths for concentration-dependent and constant dielectric permittivity. The black and red symbols and lines show the decay lengths of the total and charge density profiles at a single wall in the case of the concentration dependent permittivity.

To understand these deviations, in addition to ξ extracted from the pressure, Fig. 9b presents the decay lengths of the number and charge density profiles, ξ_p and ξ_c , at a single wall. At low concentrations, $\xi_c > \xi_p$, hence the charge density determines the leading decay length and we found $\xi \approx \xi_c$. As the concentration increases, there is a crossover to density-dominated screening, *i.e.*, $\xi_p > \xi_c$. In this regime, we obtained $\xi \approx \xi_p$. The crossover shifts toward higher concentrations as ϵ_r decreases because the decreased ϵ_r enhances the electrostatic interactions.

So far, we assumed a constant dielectric permittivity ϵ_r , while it is known that ϵ_r depends on the salt concentration ρ .^{83–87} To study how this dependence affects electrostatic screening, we considered two models with $\epsilon_r = 78$ and $\epsilon_r(\rho) = -0.031\rho^3 + 1.322\rho^2 - 13.44\rho + 80.84$, which describes the measured dielectric permittivity as a function of the concentration of NaCl at $T = 293$ K (see ref. 87). Fig. 9c shows that the concentration dependence of the relative permittivity does not affect the screening lengths at intermediate concentrations, in line with the MSA results of Rotenberg *et al.*⁴⁰ However, the crossover to the density-dominated regime is noticeably shifted towards higher concentrations. This shift is because the presence of ions reduces ϵ_r , thus enhancing the electrostatic interactions, which extends the region of the electrostatics-dominated screening.

4 Conclusions

Screening in ionic fluids is essential for many fundamental processes and industrial applications. Nevertheless, our understanding of screening in concentrated electrolytes and ILs remains incomplete. Recent SFB experiments have challenged our knowledge of screening in dense ionic systems by reporting screening lengths about one order of magnitude larger than expected. This effect was ascribed to the bulk properties of ionic systems and termed underscreening, or recently even anomalous underscreening, to pinpoint that the system is underscreened compared to what is expected based on classical theories or the



Debye ionic cloud model, respectively. We have reviewed the experimental, theoretical and simulation work attempting to resolve this apparent underscreening paradox. This overview indicates that there is no solid evidence from theory and simulations to support the (anomalous) underscreening as a bulk property of concentrated ionic systems.

New theoretical and simulation work motivated by underscreening experiments brought new insight and new questions into our understanding of ionic screening. Experiments on underscreening suggested a cubic scaling of the screening lengths with the Debye length (eqn (2) with $n = 3$). With a few exceptions,^{27,41,42} which still need careful examination, such cubic scaling has yet to be found in theory or simulations in the experimentally relevant parameter space. Instead, a selection of other scaling exponents have been reported, *viz.*, $n = 1$ (ref. 40, 41 and 58), $n = 2$ (ref. 35, 41 and 58), $n \approx 1.3$ (ref. 57), $n = 1.5$ (ref. 34, 40 and 41 and this work), and $n = 5$ (ref. 41), depending on the model and method used. Future work will show whether there is universal scaling at all, and what its physical significance is.

While reviewing the previous results on ionic screening, we noted the scarcity of studies on how solvent, ion–surface interactions and confinements influence ionic screening. We have attempted to fill this gap. We used molecular dynamics simulations at controlled chemical potential of all components and classical density functional theory to investigate how the solvent dielectric properties affect the decay length of the force exerted on the confining walls. Comparison between atomistic MD and solvent-explicit DFT simulations revealed that the solvent and ion structure differs from the behaviour in bulk – as expected – only close to the surface. Furthermore, it is – at least on a qualitative level – dominated by steric, excluded volume effects and not by ion- or surface- specific interactions, thus rendering the coarse-grained DFT calculations a viable approach to study underscreening since the usual way to control chemical composition on an atomistic resolution is computationally too demanding, and therefore infeasible. Using DFT, we found that, somewhat surprisingly, in the electrostatics-dominated regime, the screening length is virtually independent of (i) whether the solvent is modelled implicitly or is spatially resolved, (ii) whether dielectric permittivity ϵ_r depends on the ion concentration or not, and (iii) on the value of ϵ_r . However, our calculations revealed that a crossover to the hard-core dominated regime, which occurs at higher concentrations, depends sensitively on the details of the solvent (Fig. 9).

We hope this overview and our new results on the solvent effects will motivate further experimental, theoretical, and simulation work on screening in concentrated ionic systems.

Data availability

The data supporting the findings of this research, including the input scripts for the atomistic simulations, the scripts to produce the figures presented in the paper, and the custom software used in the research, are available at <https://doi.org/10.18419/darus-3551>.

Conflicts of interest

There are no conflicts to declare.



Acknowledgements

A. S., C. H. and H. J. were funded by the Deutsche Forschungsgemeinschaft (DFG, German Research Foundation) under Germany's Excellence Strategy – EXC 2075 – 390740016 and SFB 1333/2 – 358283783. S. K. acknowledges the financial support by NCN Grants 2020/39/I/ST3/02199 and 2021/40/Q/ST4/00160.

References

- 1 J. L. Seifter and H.-Y. Chang, *Physiology*, 2017, **32**, 367–379.
- 2 C. M. Armstrong, *Proc. Natl. Acad. Sci. U. S. A.*, 2003, **100**, 6257–6262.
- 3 S. Kondrat, U. Krauss and E. von Lieres, *Curr. Res. Chem. Biol.*, 2022, **2**, 100031.
- 4 S. Kondrat and E. von Lieres, in *Multienzymatic Assemblies: Methods and Protocols*, ed. H. Stamatis, Springer US, New York, NY, 2022, pp. 27–50.
- 5 B. Drukarch, H. A. Holland, M. Velichkov, J. J. G. Geurts, P. Voorn, G. Glas and H. W. de Regt, *Prog. Neurobiol.*, 2018, **169**, 172–185.
- 6 M. Peyrard, *J. Biol. Phys.*, 2020, **46**, 327–341.
- 7 M. W. Berchtold, H. Brinkmeier and M. Müntener, *Physiol. Rev.*, 2000, **80**, 1215–1265.
- 8 I. Y. Kuo and B. E. Ehrlich, *Cold Spring Harbor Perspect. Biol.*, 2015, **7**, a006023.
- 9 J. A. Rall, *Am. J. Physiol.: Adv. Physiol. Educ.*, 2022, **46**, 481–490.
- 10 A. J. Greer, J. Jacquemin and C. Hardacre, *Molecules*, 2020, **25**, 5207.
- 11 G. Kaur, H. Kumar and M. Singla, *J. Mol. Liq.*, 2022, **351**, 118556.
- 12 M. Watanabe, M. L. Thomas, S. Zhang, K. Ueno, T. Yasuda and K. Dokko, *Chem. Rev.*, 2017, **117**, 7190–7239.
- 13 G. Jeanmairet, B. Rotenberg and M. Salanne, *Chem. Rev.*, 2022, **122**, 10860–10898.
- 14 J. Wu, *Chem. Rev.*, 2022, **122**, 10821–10859.
- 15 M. Janssen, T. Verkholyak, A. Kuzmak and S. Kondrat, *J. Mol. Liq.*, 2023, **371**, 121093.
- 16 A. Paul, S. Muthukumar and S. Prasad, *J. Electrochem. Soc.*, 2020, **167**, 037511.
- 17 T. Welton, *Coord. Chem. Rev.*, 2004, **248**, 2459–2477.
- 18 H. Olivier-Bourbigou, L. Magna and D. Morvan, *Appl. Catal., A*, 2010, **373**, 1–56.
- 19 P. Attard, *Phys. Rev. E: Stat. Phys., Plasmas, Fluids, Relat. Interdiscip. Top.*, 1993, **48**, 3604–3621.
- 20 R. L. de Carvalho and R. Evans, *Mol. Phys.*, 1994, **83**, 619–654.
- 21 J. G. Kirkwood, *Chem. Rev.*, 1936, **19**, 275–307.
- 22 M. A. Gebbie, M. Valtiner, X. Banquy, E. T. Fox, W. A. Henderson and J. N. Israelachvili, *Proc. Natl. Acad. Sci. U. S. A.*, 2013, **110**, 9674–9679.
- 23 M. A. Gebbie, H. A. Dobbs, M. Valtiner and J. N. Israelachvili, *Proc. Natl. Acad. Sci. U. S. A.*, 2015, **112**, 7432–7437.
- 24 A. M. Smith, A. A. Lee and S. Perkin, *J. Phys. Chem. Lett.*, 2016, **7**, 2157–2163.
- 25 A. A. Lee, C. S. Perez-Martinez, A. M. Smith and S. Perkin, *Faraday Discuss.*, 2017, **199**, 239–259.
- 26 A. A. Lee, C. S. Perez-Martinez, A. M. Smith and S. Perkin, *Phys. Rev. Lett.*, 2017, **119**, 026002.
- 27 A. Härtel, M. Bültmann and F. Coupette, *Phys. Rev. Lett.*, 2023, **130**, 108202.
- 28 S. Kumar, P. Cats, M. B. Alotaibi, S. C. Ayirala, A. A. Yousef, R. van Roij, I. Siretanu and F. Mugele, *J. Colloid Interface Sci.*, 2022, **622**, 819–827.

29 R. Evans, R. J. F. L. de Carvalho, J. R. Henderson and D. C. Hoyle, *J. Chem. Phys.*, 1994, **100**, 591–603.

30 S. Perkin, M. Salanne, P. Madden and R. Lynden-Bell, *Proc. Natl. Acad. Sci. U. S. A.*, 2013, **110**, E4121.

31 A. A. Lee, D. Vella, S. Perkin and A. Goriely, *J. Phys. Chem. Lett.*, 2015, **6**, 159–163.

32 C. Holm and S. Kondrat, *Journal Club for Condensed Matter Physics*, 2022, DOI: [10.36471/JCCM_November_2022_02](https://doi.org/10.36471/JCCM_November_2022_02).

33 J. Zeman, S. Kondrat and C. Holm, *J. Chem. Phys.*, 2021, **155**, 204501.

34 P. Cats, R. Evans, A. Härtel and R. van Roij, *J. Chem. Phys.*, 2021, **154**, 124504.

35 R. M. Adar, S. A. Safran, H. Diamant and D. Andelman, *Phys. Rev. E*, 2019, **100**, 042615.

36 M. Han and R. M. Espinosa-Marzal, *J. Phys. Chem. C*, 2018, **122**, 21344–21355.

37 P. Gaddam and W. Ducker, *Langmuir*, 2019, **35**, 5719–5727.

38 H. Yuan, W. Deng, X. Zhu, G. Liu and V. S. J. Craig, *Langmuir*, 2022, **38**, 6164–6173.

39 T. Baimpos, B. R. Shrestha, S. Raman and M. Valtiner, *Langmuir*, 2014, **30**, 4322–4332.

40 B. Rotenberg, O. Bernard and J.-P. Hansen, *J. Phys.: Condens. Matter*, 2018, **30**, 054005.

41 A. Ciach and O. Patsahan, *J. Mol. Liq.*, 2023, **377**, 121453.

42 A. Ciach and O. Patsahan, *J. Phys.: Condens. Matter*, 2021, **33**, 37LT01.

43 O. Patsahan and A. Ciach, *ACS Omega*, 2022, **7**, 6655–6664.

44 N. G. van Kampen, *Phys. Rev.*, 1964, **135**, A362–A369.

45 C. Ebner, W. F. Saam and D. Stroud, *Phys. Rev. A: At., Mol., Opt. Phys.*, 1976, **14**, 2264–2273.

46 R. Evans, *Adv. Phys.*, 1979, **28**, 143–200.

47 Y. Rosenfeld, *Phys. Rev. Lett.*, 1989, **63**, 980–983.

48 R. Roth, R. Evans, A. Lang and G. Kahl, *J. Phys.: Condens. Matter*, 2002, **14**, 12063–12078.

49 H. Hansen-Goos and R. Roth, *J. Phys.: Condens. Matter*, 2006, **18**, 8413–8425.

50 R. Roth, *J. Phys.: Condens. Matter*, 2010, **22**, 063102.

51 S. A. Brazovskii, Phase Transition of an Isotropic System to a Nonuniform State, *30 Years of the Landau Institute – Selected Papers*, World Scientific, Singapore, 1996, vol. 11, pp. 109–113.

52 S. A. Brazovskii, *J. Exp. Theor. Phys.*, 1975, **41**, 85.

53 R. Kjellander, *Soft Matter*, 2019, **15**, 5866–5895.

54 R. Kjellander, *J. Chem. Phys.*, 2018, **148**, 193701.

55 R. Kjellander and D. J. Mitchell, *Chem. Phys. Lett.*, 1992, **200**, 76–82.

56 R. Kjellander and D. J. Mitchell, *J. Chem. Phys.*, 1994, **101**, 603–626.

57 S. W. Coles, C. Park, R. Nikam, M. Kanduč, J. Dzubiella and B. Rotenberg, *J. Phys. Chem. B*, 2020, **124**, 1778.

58 J. Zeman, S. Kondrat and C. Holm, *Chem. Commun.*, 2020, **56**, 15635–15638.

59 F. Coupette, A. A. Lee and A. Härtel, *Phys. Rev. Lett.*, 2018, **121**, 075501.

60 P. A. Bonnaud, B. Coasne and R. J.-M. Pellenq, *J. Chem. Phys.*, 2012, **137**, 064706.

61 R. W. Zwanzig, *J. Chem. Phys.*, 1954, **22**, 1420–1426.

62 A. Schlaich, A. P. dos Santos and R. R. Netz, *Langmuir*, 2019, **35**, 551–560.

63 A. Schlaich, B. Kowalik, M. Kanduč, E. Schneck and R. R. Netz, in *Computational Trends in Solvation and Transport in Liquids*, ed. G. Sutmann, J. Grotendorst, G. Gompper and D. Marx, Forschungszentrum Jülich GmbH, Jülich, 2015, vol. 28 of IAS Series, pp. 155–185.

64 E. Schneck, F. Sedlmeier and R. R. Netz, *Proc. Natl. Acad. Sci. U. S. A.*, 2012, **109**, 14405–14409.

65 M. Kanduč, A. Schlaich, A. H. de Vries, J. Jouhet, E. Maréchal, B. Demé, R. R. Netz and E. Schneck, *Nat. Commun.*, 2017, **8**, 14899.

66 H. Heinz, H. Koerner, K. L. Anderson, R. A. Vaia and B. L. Farmer, *Chem. Mater.*, 2005, **17**, 5658–5669.

67 R. Fuentes-Azcatl and J. Alejandre, *J. Phys. Chem. B*, 2014, **118**, 1263–1272.

68 P. Loche, P. Steinbrunner, S. Friedowitz, R. R. Netz and D. J. Bonthuis, *J. Phys. Chem. B*, 2021, **125**, 8581–8587.

69 D. Henderson, D.-e. Jiang, Z. Jin and J. Wu, *J. Phys. Chem. B*, 2012, **116**, 11356–11361.

70 C. E. Woodward, *J. Chem. Phys.*, 1991, **94**, 3183–3191.

71 Y.-X. Yu and J. Wu, *J. Chem. Phys.*, 2002, **117**, 10156–10164.

72 J. Wu, T. Jiang, D.-e. Jiang, Z. Jin and D. Henderson, *Soft Matter*, 2011, **7**, 11222–11231.

73 Y.-X. Yu and J. Wu, *J. Chem. Phys.*, 2002, **116**, 7094–7103.

74 Y.-X. Yu and J. Wu, *J. Chem. Phys.*, 2002, **117**, 2368–2376.

75 J. Mairhofer and J. Gross, *Fluid Phase Equilib.*, 2017, **444**, 1–12.

76 D. K. Chatteraj and K. S. Birdi, *Adsorption and the Gibbs Surface Excess*, Plenum Press, New York, 1984.

77 J. N. Israelachvili and R. M. Pashley, *Nature*, 1983, **306**, 249–250.

78 H. Sakuma, T. Kondo, H. Nakao, K. Shiraki and K. Kawamura, *J. Phys. Chem. C*, 2011, **115**, 15959–15964.

79 D. C. Grahame, *Chem. Rev.*, 1947, **41**, 441–501.

80 G. Gonella, E. H. G. Backus, Y. Nagata, D. J. Bonthuis, P. Loche, A. Schlaich, R. R. Netz, A. Kühnle, I. T. McCrum, M. T. M. Koper, M. Wolf, B. Winter, G. Meijer, R. K. Campen and M. Bonn, *Nat. Rev. Chem.*, 2021, 1–20.

81 A. M. Smith, K. R. J. Lovelock, N. N. Gosvami, T. Welton and S. Perkin, *Phys. Chem. Chem. Phys.*, 2013, **15**, 15317.

82 F. G. Donnan, *Chem. Rev.*, 1924, **1**, 73–90.

83 R. Buchner, G. T. Hefter and P. M. May, *J. Phys. Chem. A*, 1999, **103**, 1–9.

84 B. Hess, C. Holm and N. van der Vegt, *Phys. Rev. Lett.*, 2006, **96**, 147801.

85 M. Segá, S. S. Kantorovich, C. Holm and A. Arnold, *J. Chem. Phys.*, 2014, **140**, 211101.

86 M. Valiskó and D. Boda, *J. Chem. Phys.*, 2014, **140**, 234508.

87 N. Gavish and K. Promislow, *Phys. Rev. E*, 2016, **94**, 012611.

